Adsorption of Organic Dyes on Magnetic Iron Oxide Nanoparticles. Part II: Field-Induced Nanoparticle Agglomeration and Magnetic Separation

Jordy Queiros Campos, B.L. Checa-Fernandez, J. Marins, C. Lomenech, Ch. Hurel, G. Godeau, M. Raboisson-Michel, G. Verger-Dubois, A. Bee, D. Talbot, et al.

Adsorption of organic dyes on magnetic iron oxide nanoparticles. Part II: Field-induced nanoparticle agglomeration and magnetic separation

J. Queiros Campos[1], B.L. Checa-Fernandez[2,3], J. A. Marins[1], C. Lomenech[1], Ch. Hurel[1], G.Godeau[1], M. Raboisson-Michel[1,4], G. Verger-Dubois[4] A. Bee[5], D. Talbot[5] and P. Kuzhir[1*]

[1]*Université Côte d'Azur, CNRS UMR 7010 Institute of Physics of Nice (INPHYNI) – Parc Valrose 06108 Nice, France*

[2]*University of Granada, Department of Applied Physics – Avenida de la Fuente Nueva, 18071 Granada, Spain*

[3]*CEIT-Basque Research and Technology Alliance (BRTA) and Tecnun, University of Navarra, 20018 Donostia/San Sebastián, Spain*

[4]*Axlepios Biomedical – 1ere Avenue 5eme rue, 06510 Carros, France*

[5]*Sorbonne Université, CNRS, UMR 8234, PHENIX, 4 place Jussieu — 75252 Paris Cedex 5, France*

ABSTRACT

This paper (Part II) is devoted to the effect of molecular adsorption on the surface of magnetic iron oxide nanoparticles (IONP) on the enhancement of their (secondary) field-induced agglomeration and magnetic separation. Experimentally, we use methylene blue (MB) cationic dye adsorption on citrate-coated maghemite nanoparticles to provoke primary agglomeration of IONP in the absence of field. The secondary agglomeration is manifested through the appearance of needle-like micron-sized agglomerates in the presence of an applied magnetic field. With increasing amount of adsorbed MB molecules, the size of the field-induced agglomerates increases and the magnetic separation on a magnetized micropillar becomes more efficient. These effects are mainly governed by the ratio of magnetic-to-thermal energy α, suspension supersaturation Δ_0 and Brownian diffusivity D_{eff} of primary agglomerates. The three parameters (α, Δ_0 and D_{eff}) are implicitly related to the surface coverage θ of IONP by MB molecules through the hydrodynamic size of primary agglomerates exponentially increasing with θ. Experiments and developed theoretical models allow quantitative evaluation of the θ–effect on the efficiency of the secondary agglomeration and magnetic separation.

INTRODUCTION

In numerous biomedical and environmental applications of magnetic nanoparticles, like drug delivery[1-3], hyperthermia[4,5], magnetic resonance imaging[6], gene transfection[7,8], water remediation[9-11], these particles bear on their surface adsorbed molecules. At some conditions, these molecules can significantly reduce the potential barrier of interparticle interaction and provoke nanoparticle agglomeration. This is often the case for the dispersion of magnetic iron oxide nanoparticles (IONP) in physiological media[12-17], especially in blood plasma when adsorbed proteins can reduce the effective surface charge of nanoparticles or induce hydrophobic interactions promoting agglomeration[18-20]. This agglomeration affects theranostic performance of IONP, as well as their cellular uptake or biodistribution.

* Corresponding Author: pavel.kuzhir@univ-cotedazur.fr

Similar situation occurs in water remediation applications when charged pollutant species are adsorbed onto the nanoparticle surface. This is the case of the methylene blue (MB) cationic dye whose adsorption onto IONP was studied in detail in the companion paper[21] (Part I), whose results can be summarized as follows: (a) MB adsorption to oppositely charged citrate-coated IONP is found to be mostly promoted by electrostatic interactions and is very sensitive to pH variations changing the particle surface charge and to ionic strength variations tuning the interaction length scale; (b) MB is shown to form H-aggregates (pile of side-by-side stacked molecules) on the IONP surface; (c) Nanoparticles agglomerate in the presence of MB, and the agglomerate hydrodynamic size d_H exponentially increases with the surface density Q_{eq} of MB adsorbed onto the nanoparticle surface; (d) Nevertheless, the maximum surface density Q_{max} at the adsorption plateau corresponds to the packing density of a monolayer adsorbed onto each individual nanoparticle. Thus, small MB molecules (1.7×0.76×0.33 nm) are able to penetrate inside the primary agglomerates (~100–300 nm) constituted of ~10 nm sized IONP. The surface coverage is defined as $\theta=Q_{eq}/Q_{max}$ and accounts for MB embedded inside the primary agglomerates; (e) Primary agglomeration of IONP is explained by the two following mechanisms. At relatively low surface coverage θ, one expects a heterogeneous adsorption of MB molecules forming H-aggregates on the IONP surface. This creates a nonuniform surface charge distribution which could considerably lower electrostatic repulsion between particles and promote their agglomeration under van der Waals forces. This mechanism is qualitatively similar to the surface domain correlation[22]. At high surface coverage θ, the surface domain correlation is no longer relevant, but one expects that the nanoparticles are "bridged" by π-stacking aromatic interactions between two MB molecules (or two H-aggregates), each "belonging" to opposite IONP surfaces.

Whatever the mechanisms behind this primary agglomeration of magnetic nanoparticles, it is expected to considerably enhance the secondary agglomeration induced by external magnetic fields. In fact, in the considered cases, molecular adsorption promotes the appearance of primary agglomerates with a much larger size than that of individual nanoparticles. The energy of magnetic interaction between primary agglomerates is proportional to the cube of their linear dimension. Higher energy is expected to promote a stronger phase separation in the presence of a uniform magnetic field which is usually manifested through appearance of micron-sized needle-like agglomerates[23-27]. Furthermore, in non-uniform magnetic fields, these agglomerates are expected to migrate in the direction of the magnetic field gradient, thereby accelerating separation of the magnetic phase from the solvent as compared to individual non-agglomerated nanoparticles which undergo strong Brownian motion and cannot be separated from the solvent by moderate magnetic fields.

In general, magnetic separation enhanced by field-induced agglomeration is rather well documented – see reviews by Kuzhir et al.[28] and Leong et al[29]. However, the coupling between molecular adsorption, primary and secondary agglomeration and magnetic separation has received much less attention. A few existing studies are devoted to the effect of the added surfactant on the field-induced agglomeration or magnetic separation. The adsorbed surfactant molecules influence the nanoparticle stability and, consequently, the aggregation behavior under applied field through the two following effects. On the one hand, increasing surfactant concentration usually increases the IONP stability[30] and weakens or completely excludes the field-induced agglomeration. In some cases, the surfactants can screen electrostatic repulsion between nanoparticles and enhance their

primary and secondary (field-induced) agglomeration[26]. On the other hand, increasing thickness of the adsorbed molecular layer decreases magnetic interaction potential between nanoparticles and leads to a weakening of the field-induced agglomeration and to a decrease of the magnetic separation efficiency[31]. To the best of our knowledge, the effect of the surface density of the adsorbed molecules on the field-induced agglomeration or magnetic separation has never been reported.

In this paper (Part II), we discover how progressive adsorption of molecules on nanoparticle surface enhances magnetic separation of these particles. To this purpose, mixtures of citrate-coated maghemite IONP with an aqueous MB solution are used. This physicochemical system, described in the companion paper[21] (Part I), is firstly subjected to a homogenous magnetic field in order to study the field-induced agglomeration. Then, we realize magnetic separation experiments in microfluidic channels equipped with a magnetized micropillar. Under external magnetic field, the micropillar creates magnetic field gradients around himself and attracts magnetic agglomerates separating them from the suspending liquid when the magnetic colloid continuously flows through the channel[31].

The goal of the present paper is to establish experimental correlations between the surface coverage of IONP by MB and the physical parameters of the field-induced agglomeration (the average agglomerate size) and microfluidic magnetic separation (the capture efficiency). We expect that the considered pair MB/citrated IONP should allow discerning some general effects of molecular adsorption on nanoparticles agglomeration/magnetic separation valid for other adsorbent/adsorbate pairs, as long as attractive interactions between adsorbent nanoparticles induced by adsorbed molecular layers are known.

EXPERIMENTAL SECTION

IONP and MB adsorption experiments.

Detailed description of synthesis and characterization of IONP and MB adsorption experiments are provided in the companion paper[21] (Part I). Briefly, IONP were synthetized using a well-known method of co-precipitation of iron salts[32] followed by oxidation of obtained magnetite (Fe_3O_4) nanoparticles to maghemite (γ-Fe_2O_3) and their stabilization in deionized water by trisodium citrate adsorption. The adsorbed citrate ions ensured a negative electric charge on IONP surface while the colloidal stability was provided by electro-steric repulsion between nanoparticles. Individual nanoparticles have an average diameter of metal oxide cores d_M=7.6±2.7nm and an outer diameter comprising the citrate shell d_O= 8.0–9.6 nm. For experiments, the synthesized ferrofluid (colloidal suspension of IONP in a dilute aqueous solution of trisodium citrate) was diluted by either pure Milli-Q water (Millipore) or a stock water solution of MB as described in detail in Part I [ref. 21]. Amounts of mixed solutions were adjusted to get a desired molar concentration of MB, $0 \leq C_0 \leq 1$ mmol/L in the final solution, and two IONP weight concentrations were used: c_w=0.18 g/L (dilute samples labeled "SD samples") and 8 g/L (concentrated "SC samples") corresponding to IONP volume fraction of φ_0=0.0036 vol % and 0.16 vol %, respectively. The SD samples were relatively transparent and used for measurements of the hydrodynamic size distribution and the electrophoretic mobility[21] (Part I). The SC samples contain a larger iron oxide amount and were used in experiments with field-induced agglomeration and magnetic separation (the present paper –

Part II). Physicochemical parameters of these both samples without MB addition are summarized in Table S1 in Supporting Information (SI). In the absence of MB, both samples were stable for at least one month, as checked by the dynamic light scattering (DLS).

Adsorption isotherms of MB onto surface of IONP of SC and SD samples are shown in Fig. S11 of Supporting Information of Part I [ref. 21] and are satisfactorily fitted to the Langmuir adsorption law. The amount of adsorbed MB is characterized by both the surface density Q_{eq} (in mmol of adsorbed MB per gram of IONP) and the surface coverage $\theta = Q_{eq}/Q_{max}\times 100$ (in %), with $Q_{max}\approx 0.37\pm 0.01$ mmol/g being the surface density at the adsorption plateau. MB adsorption promoted primary agglomeration of IONP in the absence of the magnetic field, as tested by dynamic light scattering (DLS) on the SD samples – cf. Fig. 4b of Part I [ref. 21]. The average hydrodynamic size of the primary agglomerates increased exponentially with the surface coverage:

$$\langle d_H \rangle = d_{H0} \exp(a_0 \theta), \quad (1)$$

with $d_{H0}=17\pm 5$ nm and $a_0=6.0\pm 0.3$.

Secondary (field-induced) agglomeration and magnetic separation.

The polydimethylsiloxane (PDMS) microfluidic channels used for the secondary agglomeration (channel n°1) and magnetic separation (channel n°2) experiments were fabricated by soft photolithography as described in detail in Ezzaier et al.[31] and they are shown schematically on Fig. S1 in Supporting Information (SI). Both channels had a length of 1 cm, width of 1 mm and thickness of 200±5 µm (channel 1) or 50±3 µm (channel 2). The channel 2 was equipped with a cylindrical PDMS micropillar with embedded iron microbeads. The micropillar was placed perpendicularly to the bottom and upper channel walls spanning all the width of the channel and having a diameter $D_m=50\pm 3$µm. Flexible tubes of an internal/external diameter equal to 0.5/1 mm were introduced to both extremities of the channels to form the inlet and the outlet. In both types of experiments, the channels were filled with MB/IONP aqueous solutions, namely with SC samples at different surface coverage θ of adsorbed MB, ranging between 0 and 36%. Higher values of θ promoted relatively fast gravitational settling of the field-induced agglomerates; they were immobilized at the channel bottom, and this seriously affected their growth and magnetic separation on the micropillar.

The whole experimental setup is schematically shown on Fig. 1. In experiments with field-induced agglomeration, after filling the channel n° 1 with the MB/IONP mixture at c_w=8 g/L (φ_0=0.16 %vol), it was placed onto the stage of a transmitted light inverted microscope (Nikon Diaphot, Japan). The external magnetic field (uniform on the level of the channel) with intensities ranging between H = 1.3 and 4.7 kA/m was applied using a pair of Helmholtz coils placed around the microscope. Once the external magnetic field was switched on, the primary agglomerates (composed of numerous IONP) started to attract each other and form needle-like secondary agglomerates which became visible under the microscope several seconds upon the field application. Snapshots of the aggregation process were recorded every ten seconds for a total time of 20 min. A four-fold magnification objective and a complementary metal oxide semiconductor (CMOS) detector camera PL-B742U (PixelLink, Canada) adjusted to the microscope were used. The snapshots were then processed using ImageJ software, enabling measurement of the agglomerate length distribution with elapsed time and in function of the surface coverage θ of

adsorbed MB. The average agglomerate length L was computed at each moment of time as the first moment of the length distribution function. In addition to it, the threshold magnetic field H and the threshold IONP volume fraction φ' below which the field-induced agglomeration does not take place were measured by filling the channel n°1 with the MB/IONP samples at different IONP volume fractions φ, applying step-wise increasing values of the magnetic field intensity H for 20 min and observing whether the needle-like agglomerates of a minimal length about 1µm appear or not. The experimental dependencies $H(\varphi')$ were then plotted for different surface densities of adsorbed MB.

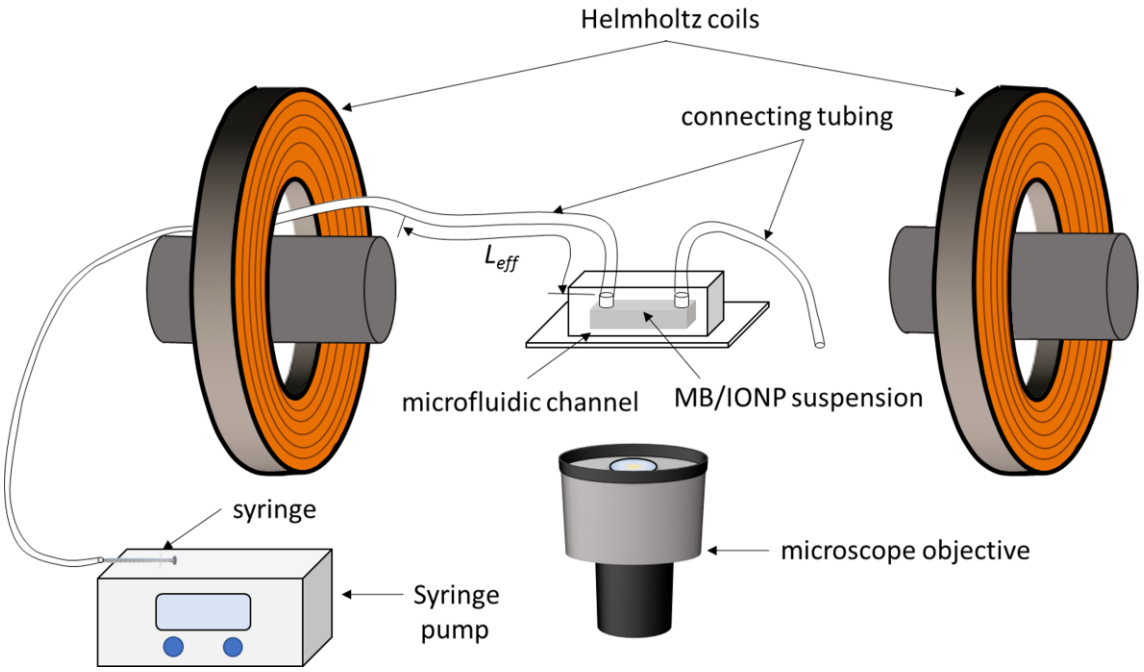

Fig. 1. Sketch of the experimental setup. A detailed scheme of the microfluidic channels with and without micropillar are shown in Fig. S1

In experiments with magnetic separation, the inlet of the channel n°2 was connected to a 5 mL syringe and was placed on the stage of the same microscope equipped with Helmholtz coils and the CMOS camera (Fig. 1). The MB/IONP mixtures at c_w=8 g/L (φ_0=0.16 %vol) and different surface coverages θ were used. The suspension flow through the channel at a desired flow rate $5 \leq Q \leq 30$ µL/min and superficial velocity $u=Q/A$ (called hereinafter flow speed, with $A=7.8\times10^{-8}$ m^2 being the channel cross-section) was induced by a syringe pump PHD Ultra (Harvard Apparatus, USA). A few minutes after the onset of the flow, an external uniform magnetic field of an intensity H=18 kA/m was applied parallel to the flow direction. The micropillar got magnetized and captured IONP (or rather their primary and/or secondary agglomerates) separating them from the suspending fluid. The IONP accumulated around the micropillar and formed micron-sized deposits extended along the applied field. The deposit growth was recorded every 10 seconds for 20 minutes. The images were then processed using the ImageJ software and the deposit area S, schematically shown on Fig. S1c was measured at each elapsed time. The relative deposit surface area, $s = 4S/(\pi D_m^{\,2})$, was finally computed as the ratio of the deposit area S to the micropillar cross-section, and was plotted as a function of the elapsed time t. The $s(t)$ dependencies allowed us to quantify the magnetic separation efficiency as a function of the surface coverage θ of the adsorbed MB.

To avoid any artefact related to possible retention of nanoparticles within the syringe, tubing or connectors, we checked several times the IONP concentration flowing out from the microfluidic channel. Using the iron dosage by Inductive Coupled Plasma Atomic Emission Spectrometry (ICP-AES, Perkin Elmer Optima 8000 DV, USA), we found the same iron concentration in the samples passed through the channel (without micropillar) as in the initial samples. All experiments were repeated twice and the reported quantities L, H and s stand for an arithmetic mean of the three measurements, while the error bars stand for the standard deviation of the values obtained in these three measurements.

RESULTS AND DISCUSSION

Aggregation threshold and phase diagram.

In these experiments, MB/IONP mixtures are placed in the microfluidic channel and their volume fraction φ and the applied magnetic field H are varied until finding the minimum magnetic field at a given volume fraction φ' required for appearance of the micron-sized needle like aggregates (cf. Experimental Section). Note that φ' (IONP volume fraction at aggregation threshold) should not be confounded with φ (IONP volume fraction beyond the threshold). Experimental dependencies $H(\varphi')$ are plotted in Fig. 2a for different values of the surface coverage θ. We clearly observe that for each θ, the threshold magnetic field intensity decreases with increasing IONP volume fraction because shorter distances between primary agglomerates at increasing φ' promote stronger dipolar interactions between them such that lower magnetic field is required to induce the field-induced agglomeration[33-35]. In general, $H(\varphi')$-curves in Fig. 2a correspond to binodal decomposition of the magnetic colloid and the whole figure can be seen as a part of the phase diagram. For a fixed value of θ, the dilute phase without needle-like agglomerates is situated on the left side of the curve $H(\varphi')$ corresponding to the given θ, the mixture of the concentrated (needle-like agglomerates) and dilute (the medium surrounding the needle-like agglomerates) phases is situated on the right of the curve, while the concentrated phase and the second binodal curve are not accessible in the present experiments.

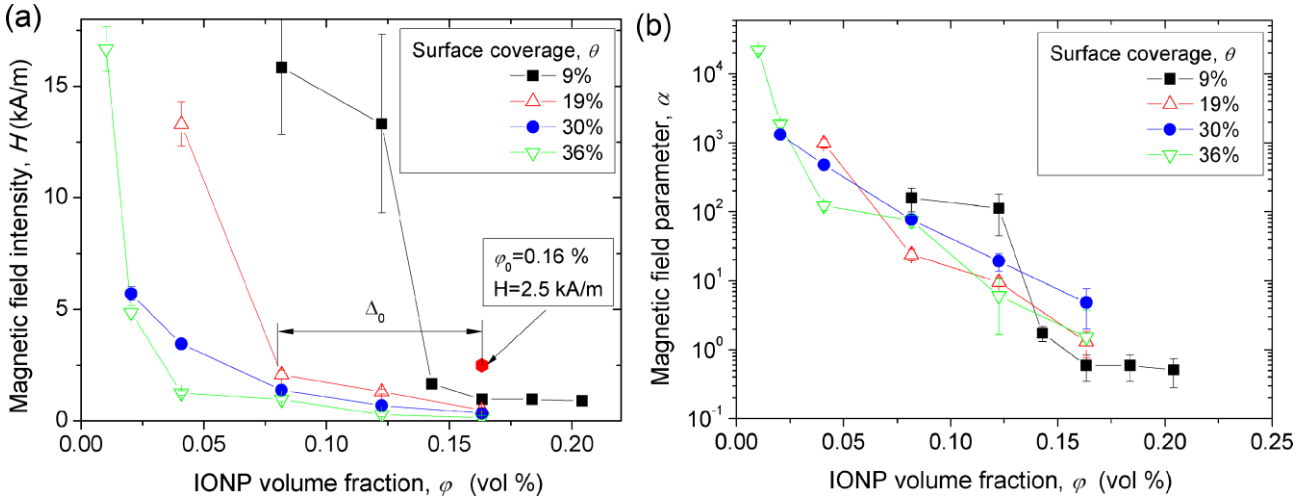

Fig. 2. Phase diagrams of the MB/IONP suspensions at different surface coverages by MB, plotted in $H-\varphi$ (a) or $\alpha-\varphi$ (b) coordinates. All plotted $H(\varphi')$ or $\alpha(\varphi')$-curves correspond to the aggregation threshold. The suspension supersaturation Δ_0 is graphically represented on (a) for a particular case of the initial IONP volume fraction φ_0=0.16 vol%, the applied magnetic field H=2.5 kA/m and the MB surface coverage θ=19%.

As also seen from Fig. 2a, the $H(\varphi')$ curves and consequently the agglomeration threshold are shifted to lower IONP volume fractions when increasing the amount of adsorbed MB. Such effect can be easily understood in terms of increasing magnetic dipolar interactions between primary agglomerates, as their effective size $<d_H>$ (average hydrodynamic diameter measured by DLS) increases with increasing surface coverage[21] [Eq. (1); Fig. 4b in Part I]. From the theoretical perspective, the field-induced agglomeration is governed by the interplay between the energy of magnetic dipolar interactions between primary agglomerates[36] (of identical diameters d_H), $U_d \sim m^2/(\mu_0 d_H^3)$ and the thermal agitation energy k_BT ($\approx 4\times10^{-21}$ J at room temperature), with $\mu_0 = 4\pi\times10^{-7}$ H/m being the magnetic permeability of vacuum; $m=\mu_0 Mv \sim \mu_0\beta H d_H^3$ – the magnetic moment of magnetizable agglomerates of a volume v; $\beta=(\mu-1)/(\mu+2)$ is the agglomerate magnetic contrast factor assuming its spherical shape; μ and M – its relative magnetic permeability and magnetization evaluated in a linear magnetization limit appropriate for the considered range of magnetic fields. Because of a broad size distribution of the primary agglomerates, it is convenient to consider the quantities $<m>$ and $<d_H^3>$ averaged over the size distribution in the definition of U_d. The ratio of these both energies is hereinafter called the magnetic field parameter. It takes the following form (quite similar to the previous work[37]) for the experimentally observed log-normal size distribution:

$$\alpha = \frac{\mu_0\beta^2 H^2 \left\langle d_H^6 \right\rangle}{k_B T \left\langle d_H^3 \right\rangle} = \frac{\mu_0\beta^2 H^2 \left\langle d_H \right\rangle^3}{k_B T} \exp(12\sigma^2) \qquad (2)$$

with $\sigma \approx PDI^{1/2}$ being the dimensionless size distribution width and PDI – the polydispersity index revealed by DLS [Fig. 4b in Part I]. From this definition, it is clear that at fixed external magnetic field H, θ affects α through the average hydrodynamic size $<d_H>$ of primary agglomerates, the size distribution width σ and the magnetic contrast factor β. The first one ($<d_H>$) increases exponentially with the surface coverage θ [Eq. (1)], the second one (σ) experiences a moderate increase with θ [Fig. 4b in Part I], while the last one (β) slightly decreases with θ because the adsorbed MB monolayer slightly increases the distance between iron oxide cores of nanoparticles, which decreases the volume fraction of magnetic material per agglomerate, decreases dipolar interactions between IONP and, consequently, the magnetic permeability μ of the agglomerate. Indeed, using a modified second-order modified mean-field (MMF2) theory[38], we evaluate that MB monolayer of a thickness 0.76 nm (reported in Part I) decreases the contrast factor from β=0.92 at θ=0 to β=0.87 at θ=1. Therefore, this latter effect can be neglected, while the exponential growth of $<d_H>$ can be considered as a dominant contribution of θ to the magnetic field parameter α. Putting $\beta \approx \text{const} \approx 1$, the expression for α [Eq. (2)] is written in its final form as follows:

$$\alpha \approx \frac{\mu_0 H^2 \left\langle d_H \right\rangle^3}{k_B T} \exp(12\sigma^2). \qquad (3)$$

We tempt therefore to renormalize the phase diagram shown in Fig. 2a using the magnetic field parameter α [Eq. (3)] instead of the magnetic field intensity H. Experimental dependences $\alpha(\varphi')$ are shown in Fig. 2b and appear to more or less collapse onto a single curve for all the values of the surface coverage θ, except for a few points at θ=9% (corresponding to the largest errors on the quantities of adsorbed MB). Such collapse indicates that the secondary field-induced

agglomeration is mostly governed by magnetic interactions between primary agglomerates, and α is the only governing parameter. This is consistent with evaluation of the van der Waals interaction between primary agglomerates that is 4.5 – 110 times lower than magnetic one at θ=9 – 36%.

Secondary (field-induced) agglomeration.

In these experiments, the magnetic field is applied to the MB/IONP mixtures (SC samples) at the elapsed time t_0=1 h after MB/IONP mixing. This time is larger than the characteristic time of MB adsorption[21] (<30 min, cf. Fig. S9 of Part I), so that the adsorption kinetics does not interfere with the kinetics of the field-induced agglomeration. Once the external magnetic field is on, the primary agglomerates get magnetized and form needle-like secondary agglomerates extended along the magnetic field direction and whose size increases progressively with time. The snapshots of the secondary agglomerates taken at the elapsed time (after the field application) t=20 min for the magnetic field intensity H=2.5 kA/m and for the samples of four different surface coverages θ are shown in Fig. 3, while the whole set of snapshots at different elapsed times and at three different magnetic fields are presented in Figs. S2 and S3. Some gray objects visible on the left snapshot at θ=0 correspond to dust adhered to the bottom of the channel, while the macroscopic appearance of the sample remained the same before, during and after the magnetic field application. This allows claiming that the field-induced agglomeration is not observed in the absence of MB or, strictly speaking, the size of the secondary agglomerates (if they exist) is below the resolution limit of our optics (about 1μm). At $\theta \geq 9\%$, the size of the needle-like agglomerates increases progressively with increasing surface coverage θ of adsorbed MB. It is worth noticing that the field-induced agglomeration in the presence of MB is totally reversible with respect to the magnetic field application: once the field is off, the secondary agglomerates dissociate.

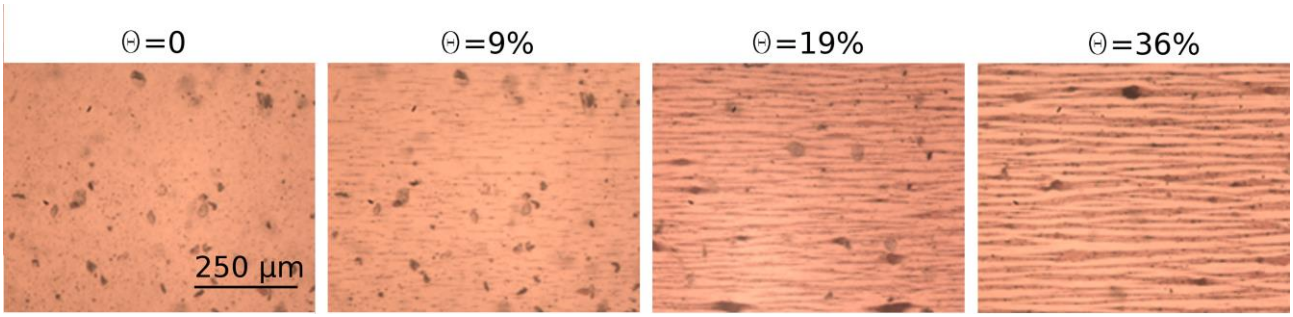

Fig. 3. Snapshots of the SC-MB samples showing the field-induced (secondary) agglomeration at H=2.5 kA/m and the elapsed time t =20 min. IONP concentration is c_w=8 g/L, φ_0=0.16 %vol.

The driving force of the field-induced agglomeration is the difference of the initial volume fraction φ_0 of IONP before the phase separation starts and the volume fraction φ' at the aggregation threshold, $\Delta_0 = \varphi_0 - \varphi'$, referred to as initial supersaturation. The magnitude Δ_0 is represented graphically on Fig. 2a for a particular case of θ=19%, H=2.5 kA/m and φ_0=0.16%.

To quantify the field-induced agglomeration, we have measured the distribution of agglomerate lengths at different elapsed times [Fig. S4]. It should be noted that our experimental setup does not allow detecting the aggregates of the size lower than ~1 μm. However, the recent theoretical model[39] predicts a considerable increase of the minimal agglomerate size with time such that nanosized aggregates likely disappear at elapsed times t approximately larger that the agglomeration timescale τ_a (determined below). We believe therefore that the chosen optical

microscopy method gives a relevant picture of the aggregate size distribution at least at times $t \geq \tau_a$. For more precise determination of the size distribution of small aggregates, light scattering experiments, like the ones described in refs. 24 and 40, could be conducted in future. The measured size distribution allows computing the average agglomerate length L (see Experimental Section for details) which is plotted as function of the elapsed time t in Fig. 4a for a fixed magnetic field H=2.5 kA/m and three values of the surface coverage θ and in Fig.4b for a fixed surface coverage θ=9% and three different values of H. As is seen form these both figures, the agglomerate size progressively increases with time and seems to approach a horizontal plateau at t>800 s. In reality, at such long times, we start observing coalescence of the neighboring agglomerates and the length of certain agglomerates becomes larger than the width of the observation window, so that these large agglomerates are excluded from the size distribution. At such condition the observed plateau cannot be associated to the final size of the agglomerates but rather corresponds to a transition between the growth stage and the coalescence stage of the field-induced agglomeration, as pointed out by Ezzaier et al.[25] During the growth stage, the secondary agglomerates absorb individual primary agglomerates from the dilute phase and grow until the thermodynamic equilibrium between the concentrated and dilute phases is fully established when the plateau is reached. We also observe that the maximum agglomerate length L_{max} at the plateau increases gradually with both the surface coverage θ of the adsorbed MB [Fig. 4a] and the magnetic field H [Fig. 4b].

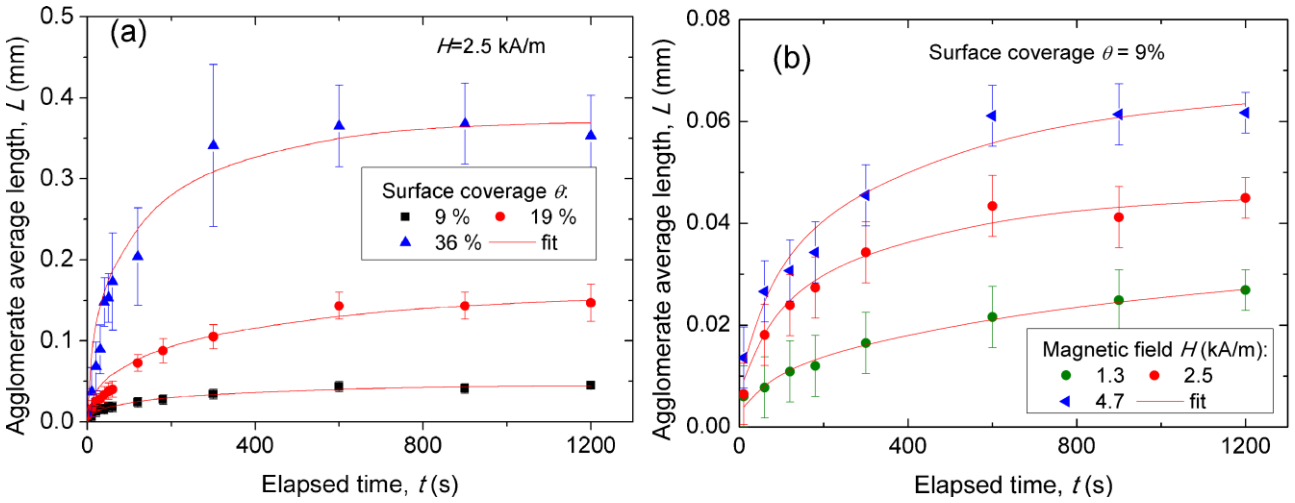

Fig. 4. Dependencies of the average length of field-induced agglomerates on the elapsed time for the SC samples at: (a) different surface coverage θ and fixed magnetic field H=2.5 kA/m, and (b) different magnetic fields H and fixed surface coverage θ=9%. IONP concentration is c_w=8 g/L, φ_0=0.16 %vol.

It is worth noticing that the confinement of the MB/IONP suspension in a narrow channel could in principle influence the field-induced agglomeration. In particular, the needle-like agglomerates could develop a repulsive interaction with the bottom and upper channel walls arising due to confinement of the magnetic field lines in the gap between the secondary agglomerate and the wall creating a higher pressure in this gap (filled with a dilute suspension of primary agglomerates) than on the other side of the agglomerate. This effect considered in Ezzaier et al.[25] is similar to the levitation of magnetic bodies in a ferrofluid[36] and could explain the absence of gravitational settling of the secondary agglomerates in our experiments. However, the length scale of this interaction is on the order of the agglomerate thickness, so that the wall interaction should not affect the size distribution and the kinetics of aggregation if the agglomerate thickness remains much smaller than the channel width – the case of our experiments. A few measurements conducted at the channel

widths 50, 100 and 200 μm did not reveal any significant difference in aggregation behavior. This allows us supposing that confinement effects do not appear in our experimental range of parameters.

Prediction of the aggregate size evolution.

For a deeper understanding of the effect of the surface coverage θ on the kinetics of the secondary agglomeration, let us try to predict the shape of the $L(t)$ dependency using the model of the growth stage developed in our previous works[24,35]. Since the magnetophoretic flux gives a negligible contribution to the agglomeration process in the considered range of the magnetic field parameter α, the kinetic equation describing the agglomerate volume (V) growth takes the form:

$$\varphi'' \frac{dV}{dt} \approx 2\pi \frac{L}{\ln(r_a)} D_{eff} \Delta, \tag{4a}$$

$$\Delta = \Delta_0 - \varphi'' n_a V, \tag{4b}$$

where φ'' is the IONP volume fraction inside the field-induced agglomerates, r_a is their length-to-diameter ratio, $D_{eff} = k_B T / (3\pi\eta \langle d_H \rangle)$ is the effective translational diffusivity of the primary agglomerates (directly assessed by DLS), Δ is the suspension supersaturation at a given time t, n_a is the number of field-induced agglomerates per unit volume (assumed to be constant with time and equal to the number of critical nuclei at the end of the very fast nucleation stage), η=10^{-3} Pa×s is the solvent (water) viscosity. The parameters φ'' and n_a are not easily accessible in our experiments. Equation (4b) directly gives us the maximum volume V_{max} of agglomerates at the end of the growth stage, when Δ=0:

$$V_{\max} = \frac{\Delta_0}{\varphi'' n_a}. \tag{5}$$

The equation (5) shows that the maximum volume V_{max} (and consequently, the maximum length L_{max}) is an increasing function of the initial supersaturation Δ_0. Since Δ_0 increases progressively with the surface coverage θ of adsorbed MB and with the magnetic field H, the agglomerate size also increases with θ and H, as confirmed by experiments – see Table I where experimental values of L_{max} and Δ_0 are summarized for different θ and H.

Table I. Characteristics of the secondary (field-induced) agglomerates

Fixed magnetic field H=2.5 kA/m (Fig. 4a)				Fixed surface coverage θ = 9% (Fig. 4b)			
θ (%)	9	19	36	H (kA/m)	1.3	2.5	4.7
$\langle d_H \rangle$ (nm)	25.8	53.3	129	$\langle d_H \rangle$ (nm)	25.8	25.8	25.8
Δ_0 (%)	0.019	0.08	0.13	Δ_0 (%)	0.005	0.019	0.022
L_{max} (μm)	46±1	159±7	371±10	L_{max} (μm)	38±3	46±1	66±3
τ_a (s)	422 ±88	571 ±117	262 ±48	τ_a (s)	1960 ±480	422 ±88	506 ±130

Analysis shows that at practically relevant elapsed times (t >10 s), the magnitudes L and r_a vary with elapsed time much slower than Δ. This allows replacing L and r_a in Eq. (4a) by their

maximal values L_{max} and r_{max}. Integrating Eq. (4a) making use of Eqs. (4b) and (5), we get the following simple expression for the agglomerate volume as function of time:

$$V(t) = V_{\max}\left[1-\exp(t/\tau_a)\right], \tag{6a}$$

$$\tau_a = \frac{\varphi'' V_{\max}\ln(r_{\max})}{2\pi D_{eff} L_{\max}\Delta_0} \propto \frac{\varphi'' D_{\max}^{\ 2}}{D_{eff}\Delta_0}, \tag{6b}$$

where τ_a is the characteristic timescale of the field-induced agglomeration and D_{max} is the average agglomerate thickness at the end of the growth stage. The temporal evolution of the average agglomerate length $L(t)$ can be obtained from $V(t)$ dependency [Eq. (6a)] if the relationship between L and V is known. Minimization of the agglomerate free energy provides the approximate expression[25] $L \sim \delta^{-2/7} V^{3/7}$ (δ is a characteristic thickness of the agglomerate interface layer, on the order of the "outer" diameter d_O=8.0-9.6 nm of individual nanoparticle), which results in the following theoretical $L(t)$ dependency:

$$L^{7/3} = L_{\max}^{\ 7/3}\left[1-\exp(t/\tau_a)\right]. \tag{7}$$

All the experimental curves in Figs. 4a and 4b have been fitted by Eq. (7) with two adjustable parameters L_{max} and τ_a. Equation 6 seems to satisfactorily fit the experimental data (red lines in Fig. 4) and the values of the fitting parameters are reported in Table I along with the experimental values of Δ_0 at different θ and H. If the growing tendency of L_{max} with increasing values of θ and H is rather clear (as discussed above), the variation of the characteristic time with θ and H appears to be less clear. The difference in τ_a values for θ=9% and 19% (at fixed H=2.5 kA/m) and for H= 2.5 kA/m and 4.7 kA/m (for fixed θ=9%) falls within the error of the fit. On the other hand, τ_a values are considerably smaller for the highest surface coverage θ=36% as compared to θ=9% and for the highest magnetic field H=4.7 kA/m as compared to H=1.3 kA/m. We can thus think about globally decreasing trend of τ_a as a function of θ and H.

From the theoretical point of view, the characteristic timescale [Eq. (6b)] is expected to decrease with initial supersaturation ($\tau_a \propto \Delta_0^{-1}$), and consequently with the surface coverage θ and the field H. On the other hand, with increasing θ, the hydrodynamic size of the primary agglomerates increases[21] [Table I, Eq. (1) and Fig. 4b in Part I] and their diffusion becomes slower which should slow down the field-induced agglomeration ($\tau_a \propto D_{eff}^{-1}$). However, under applied field, the primary agglomerate likely changes its porosity and shape that can affect its diffusivity. Finally, with increasing θ and H, the agglomerate thickness seems to increase, which could further slow down the growth of the agglomerates ($\tau_a \propto D_{\max}^{\ 2}$). Thus, the agglomeration timescale comes from the competition between these three effects, and the first one seems (Δ_0-effect) to dominate, at least, for the highest considered surface coverage and magnetic field. Quantitative prediction of $L_{max} \sim \delta^{-2/7} V_{\max}^{\ 3/7}$ and τ_a using Eqs. (5) and (6b) is unfortunately hardly possible because of large uncertainties or impossibility of the experimental evaluation of the parameters D_{max}, δ and φ'' associated to the secondary agglomerates, as well as the diffusivity D_{eff} of the primary agglomerates in case of the morphological changes under applied field.

It is worth noticing that polydispersity of primary agglomerates can seriously influence the secondary agglomeration. In particular, the polydispersity decreases the aggregation threshold, i.e. minimal magnetic field required to onset the field-induced agglomeration at a given IONP concentration. This could be easily demonstrated through the definition of the magnetic field parameter [Eq. (3)] showing an exponential growth with the dimensionless distribution width σ. Since the aggregation threshold depends only on α (as inferred from Fig. 2b), higher polydispersity of primary agglomerates (higher σ values) will lead to lower threshold magnetic field at the same threshold value of α. On the contrary, at a fixed magnetic field H in kinetic experiments, increasing α values with the increase in the distribution width σ is expected to lead to an increase of the suspension supersaturation Δ_0 and, consequently, to a faster field-induced agglomeration and larger agglomerate size, as inferred from Eqs. (5) and (6b). These expectations are understood from the general consideration that the energy of the magnetic dipolar interaction between particles scales with the cube of the particle size, so that a small amount of larger particles (present in a polydisperse sample) aggregate much easier and faster under an applied field than a large amount of smaller particles of a monodisperse sample. Indeed, Vinod and Philip[41] have experimentally confirmed that increasing polydispersity at a fixed average nanoparticle size lead to a faster and stronger aggregation under applied field. The same effects are recovered by a bidisperse approximation[42] of the phase equilibrium model of a magnetic colloid.

From the practical point of view, it can be learned that the micron-sized field-induced agglomerates already appear at the elapsed time as small as t~1 min [Fig. 4] even though the characteristic timescale τ_a of the agglomerate growth varies between about 5 and 30 min [Table I]. This is a starting point for the magnetic separation study, in which the travel time of IONPs along the connecting tubing subjected to the magnetic field should be at least not smaller than 1 min in order to leave enough time to the primary agglomerates to form secondary needle-like structures which must considerably enhance the separation efficiency.

Magnetic separation.

In these experiments, the MB/IONP mixtures (SC samples) were pushed through the microfluidic channel and, in the presence of an external uniform magnetic field H=18 kA/m created by the Helmholtz coils. A large part of the tube connecting the syringe pump with the microfluidic channel passes inside the coils, with L_{eff}≈15 cm being an effective tubing length subject to the uniform magnetic field created by the Helmholtz coils [Fig. 1]. In most cases, the secondary (field-induced) agglomerates already appeared inside the connecting tubing well before arriving to the microfluidic channel. In the presence of the external field, the micropillar inside the microfluidic channel got magnetized, created a gradient magnetic field around himself and started capturing the primary and secondary agglomerates composed of IONP with adsorbed MB on their surface. The snapshots showing the deposits of the IONP around the micropillar at two different flow rates Q, for three different values of the surface coverage θ by MB molecules and at the elapsed time t=20 min from the moment of the magnetic field application are shown in Fig. 5, while the whole set of snapshots at different elapsed times and for different flow rates is presented in Fig. S5. The first row of Fig. 5 shows naked micropillars at elapsed time t=0 (or rather their view from the top, the micropillars being perpendicular to the observation plain and thus appearing as circles). We can clearly see, that in the presence of the magnetic field, the deposits of captured IONP have an extended shape along the magnetic field and the flow direction and show a considerable asymmetry with respect to the

flow direction: the size of the deposits attached to the micropillar surface facing the flow is larger than the size of the deposits on the opposite direction. Such shape effects have been studied in detail in our previous works[31,37] and in the present paper we focus the main attention on the effect of the adsorbed MB layers on the IONP surface on the magnetic separation process. Notice that in the absence of MB (θ=0, snapshots not shown), the applied magnetic field of an intensity H=18 kA/m appears to be too low and no any capture of isolated IONP is observed at the scale of ~1 μm corresponding to optical resolution in our experiments. On the other hand, in the presence of MB, the formation of deposits is fully reversible with respect to magnetic field application: once the field is removed, the deposits completely dissociate under Brownian motion even in the absence of flow.

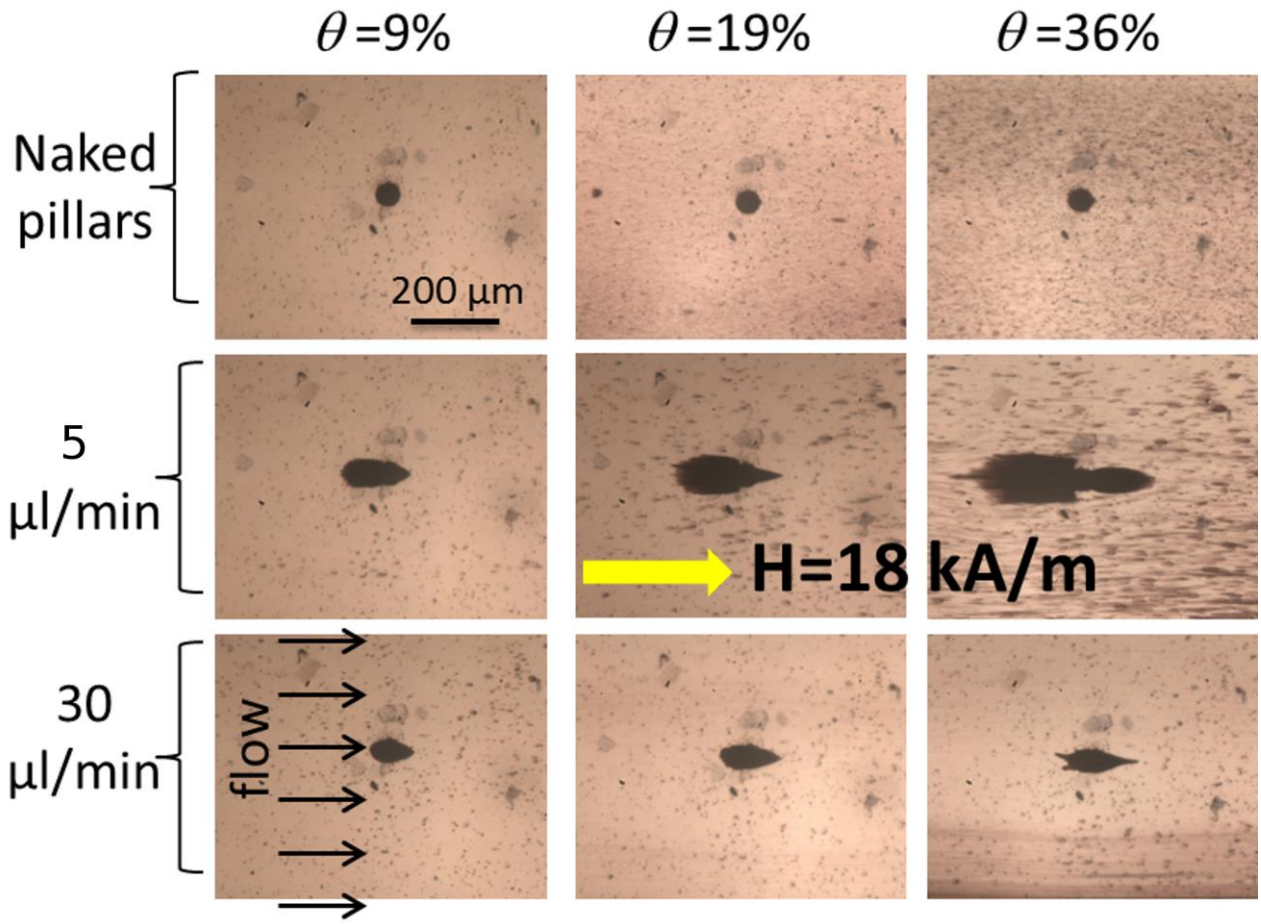

Fig. 5. Snapshots of the magnetic separation of the MB/IONP mixture (SC-sample) on a magnetizable micropillar under flow through a microfluidic channel in the presence of an external magnetic field H=18 kA/m. The first row shows naked micropillars in the beginning of the separation (t=0), the second and the third rows show the capture of IONP by the micropillar at t=20 min and at the flow rates Q=5 and 30μl/min. IONP concentration is c_w=8 g/L, φ_0=0.16 %vol.

To quantify this process, we measured the relative area s of the deposits [cf. Experimental Section for definition] at different elapsed times t, and we plot the $s(t)$ experimental dependencies in Fig. S6 for different values of θ and Q. Following the protocol described in details in Ezzaier et al.[31], we fit each of these curves by a semi-empirical function $s(t) = s_{\max}\left[1-\exp(t/\tau_s)\right]$ describing the kinetics of the deposit growth around a micropillar, with two adjustable parameters s_{max} and τ_s having a meaning of the maximum deposit area (corresponding to the maximal amount of IONP that the micropillar can retain before the erosive hydrodynamic forces rupturing the particles from the deposit surface start to dominate over the attractive magnetic forces) and characteristic

timescale of the magnetic separation. In filtration studies, it is common to introduce a capture efficiency Λ as a ratio of the flux of IONP captured by the micropillar at the beginning of the magnetic separation to the convective flux $\varphi_0 u D_m h_m$ arriving to the projected area $D_m h_m$ of the micropillar, where φ_0 =1.6×10^{-3} (0.16% vol) is the IONP volume fraction in SC samples, D_m =50 μm and h_m =50 μm are the micropillar diameter and height and $u=Q/A$ is the flow speed [cf. Experimental Section]. The capture efficiency is related to the separation timescale through the following expression: $\Lambda = \pi\varphi'' s_{\max} D_m / (4\varphi_0 u \tau_s)$, where for definiteness we take a value $\varphi'' \approx 0.7$ (70% vol) for the IONP volume fraction inside the deposits (this value does not have any importance on the effect of θ on Λ as long as φ'' is considered constant for any θ). Both parameters s_{max} and Λ describing the magnetic separation are expected to depend on the interplay between hydrodynamic F_H and magnetic F_M forces acting on IONP described by the Mason number, defined in the linear magnetization limit as[43]

$$Ma = \frac{F_H}{F_M} \approx \frac{\eta u D_m}{\mu_0 H^2 d_M^2}. \qquad (8)$$

Here, we take the metal core diameter d_M of individual IONP as a characteristic dimension of the suspension structural units, bearing in mind that the capture efficiency Λ rather depends on the size of the field-induced agglomerates, as taken into account in the model developed below. The choice for d_M allows defining the Mason number independent of the surface coverage θ, such that the effect of θ on the capture efficiency Λ is better visualized by comparison of $\Lambda(Ma)$-curves plotted at different θ.

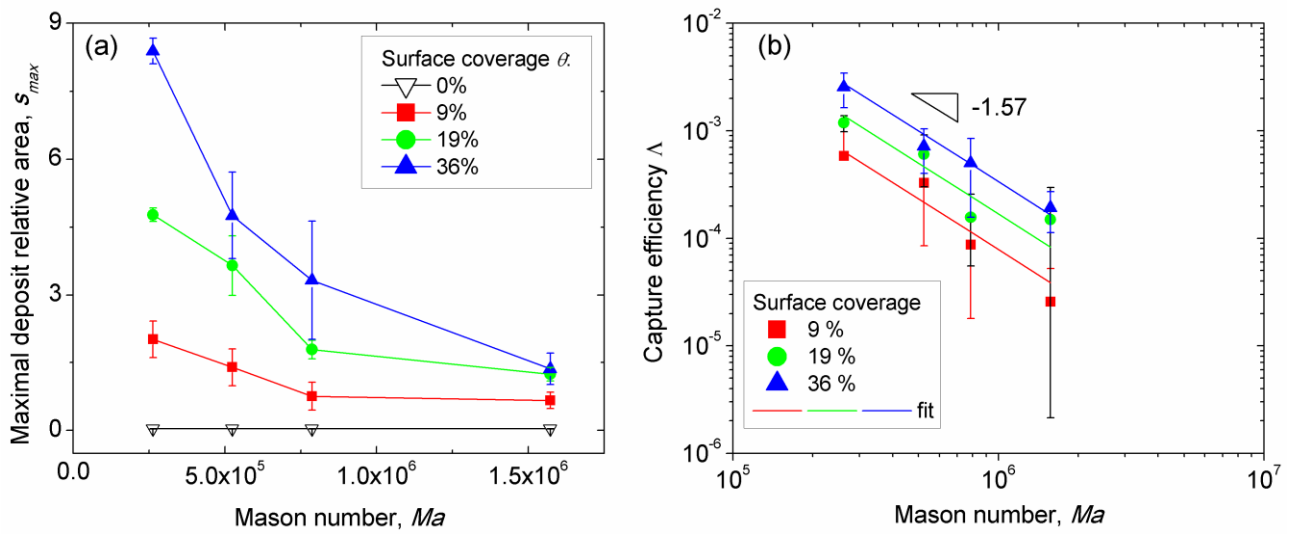

Fig. 6. Mason number dependencies of the maximal deposit relative area (a) and the capture efficiency (b) for the MB/IONP mixtures (SC samples) at different surface coverage θ and at the magnetic field H=18 kA/m. IONP concentration is c_w=8 g/L, φ_0=0.16 %vol.

The maximal relative deposit area s_{max} and the capture efficiency Λ are plotted as a function of the Mason number on Figs. 6a and 6b. We see that both s_{max} and Λ parameters are decreasing functions of the Mason number, which is consistent with the fact that increasing hydrodynamic forces rupture IONP more easily from the surface of the deposits and make the particle capture on the micropillar more difficult. Furthermore, both parameters s_{max} and Λ progressively increase with the surface coverage θ of MB molecules adsorbed onto the IONP surface, which is qualitatively consistent with

the fact the MB adsorption promotes the primary and secondary field-induced agglomeration, which increases magnetic attraction to the micropillar. The horizontal black line with s_{max}=0 in Fig. 6a corresponds to the absence of any distinguishable particle capture in the absence of MB (θ=0).

Scaling law for the capture efficiency.

For the deeper understanding of the surface coverage effect on the magnetic separation efficiency, let us adapt the previously developed theoretical model[31] to evaluate the capture efficiency Λ as function of the Mason number. First, we have to be sure that the traveling time t_{tr} of the MB/IONP suspension through the circuit is large enough for the field-induced agglomerates to appear. Recall that a part of the connecting tubing of an effective length L_{eff}=15 cm is subject to the external magnetic field [Fig. 1]. The traveling time is dominated by the flow through the connecting tubing rather than through the short microfluidic channel. It is evaluated as follows: $t_{tr}=V_t/Q=A_tL_{eff}/Q=\pi D_t^2L_{eff}/(4Q)\approx$80-470 s, where V_t, A_t and D_t=0.5 mm are the tubing volume, cross-section and diameter, respectively. This travel time appears to be comparable to the timescale of the secondary agglomeration ($\tau_a\approx$260-570 s for H=2.5 kA/m, cf. Table I; τ_a is expected to be shorter for a higher field H=18 kA/m in magnetic separation experiments).

Second, the IONP agglomerates traveling through the tube are subjected to the shear field of the Poiseuille flow that could promote shear-induced agglomeration. To check this effect, we keep in mind that the connecting tubing is mostly aligned with the external magnetic field, thus, the elongated secondary agglomerates should be parallel to the main flow through the tube. We compare the convective flux of smaller primary agglomerates toward the larger secondary ones[44], $J_{conv}=D^3\gamma\varphi/6$ with the diffusive flux – cf. right hand side of Eq. (4a) – $J_{diff}=2\pi LD_{eff}\Delta/\ln r_a$, with their ratio defined as the Peclet number:

$$Pe\approx\frac{D^3\gamma\ln r_a}{12\pi LD_{eff}}, \tag{9}$$

with D and L being the diameter and the length of the secondary agglomerates, $\gamma=(2/3)\gamma_w=64Q/(3\pi D_t^3)$ - the average shear rate over the tube cross-section, γ_w - wall shear rate. The Peclet number is evaluated to fit the interval 0.05<Pe<0.3 in the considered range of experimental parameters. On the basis of these two evaluations (t_{tr} and Pe), we can consider that the field-induced agglomeration of the primary agglomerates dominates the shear-induced agglomeration under the shear rate of the Poiseuille flow through the connecting tubing. At this point, it is important to notice that the diffusive particle flux is decisive in the field-induced agglomeration because the particle concentration outside the aggregate in a close proximity to its surface appears to be smaller than the concentration far from the aggregate – a common issue of condensation phase transitions – as has been studied in details by Zubarev and Ivanov[45] and Ezzaier et al.[25]. In this context, the Peclet number remains an appropriate criterion for the comparison of flow-induced with field-induced agglomeration, as inferred from the recent work[46].

Third, we have to keep in mind that the flowing IONP suspension always contains both primary and secondary agglomerates, as inferred from the phase diagram on Fig. 2a. We have to check the relative contributions of these two types of agglomerates to the global capture efficiency. These contributions read: $\Lambda_1\approx(\varphi/\varphi_0)(\langle d_H\rangle/d_M)^2\Lambda_0$ for the primary agglomerates[47], and

$\Lambda_2 \approx (1-\varphi/\varphi_0)(D/d_M)^2\Lambda_0$ for the secondary ones[31], where Λ_0 is the capture efficiency of individual nanoparticles of a metal core diameter d_M. The volume fraction of the primary agglomerates φ can be evaluated as function of the traveling time making use of Eqs. (4) – (6): $\varphi(t_{tr}) = \varphi' + \Delta(t_{tr}) = \varphi' + \Delta_0 \exp(-t_{tr}/\tau_a)$, where the values of the initial supersaturation Δ_0 and the concentration φ' at the agglomeration threshold can be retrieved from the experimental phase diagram [Fig. 2a] as function of the surface coverage θ, while the agglomeration timescale τ_a can be evaluated using the values in Table I. Evaluations show that Λ_2 contribution is at least two orders of magnitude higher than Λ_1, meaning that the major mass of the captured IONP comes from secondary agglomerates. This was expected because the capture efficiency is proportional to the square of the agglomerate diameter ($<d_H>$ or D) in both cases of spherical primary and needle-like secondary agglomerates, with D being typically much larger than $<d_H>$.

Thus, neglecting the contribution of the primary agglomerates and taking into account that $\Lambda_0 \propto Ma^{-1}$ [cf. ref. 47], the capture efficiency scales as[31]:

$$\Lambda \approx \Lambda_2 \propto (D/d_M)^2 Ma^{-1}. \tag{10}$$

Here we have omitted the term $(1-\varphi/\varphi_0)$ because its variation with the traveling time appears to be much less important than that of D^2. The average thickness D of the secondary agglomerates is related to its volume through $D \propto V^{2/7}$ under assumption of the free energy minimum on the scale of one agglomerate. Since the field-induced agglomeration happens at the same time as the suspension flows through the connection tubing, the secondary agglomerates are expected to grow when traveling along the tube and their size is expected to progressively increase with the traveling time $t_{tr}=A_tL_{eff}/Q=A_tL_{eff}/(Au)$, recalling that $A=7.8\times10^{-8}$ m^2 is the cross-section of the microfluidic channel [Experimental Section]. Assuming the same kinetics of agglomeration as in the absence of flow [Eq. (6a)] and keeping only the leading order expansion on t_{tr}/τ_a (acceptable approximation for development of a scaling law), the agglomerate thickness evolves with the travel time as:

$$D = D_{\max}\left[1-\exp\left(\frac{t_{tr}}{\tau_a}\right)\right]^{2/7} \approx D_{\max}\left(\frac{A_tL_{eff}}{Au\tau_a}\right)^{2/7}. \tag{11}$$

Substituting Eq. (11) into Eq. (10), one obtains the scaling law for Λ in its final form:

$$\Lambda \propto \left(\frac{D_{\max}}{d_M}\right)^2\left(\frac{A_tL_{eff}}{Au\tau_a}\right)^{4/7} Ma^{-1} \propto \frac{{D_{\max}}^2}{(\alpha\tau_a)^{4/7}} Ma^{-11/7}, \tag{12}$$

where, in order to get the scaling law in terms of governing dimensionless parameters, the flow speed has been expressed as $u \propto \alpha Ma$. The right-hand side of Eq. (12) underlines the fact that the capture efficiency scales with $Ma^{-11/7}$ (or $Ma^{-1.57}$) only at the fixed magnetic field H (or at fixed α). Also, in the pre-factor at $Ma^{-11/7}$, only the magnitudes important for further analysis are kept, and this pre-factor is not dimensionless. Experimental dependencies $\Lambda(Ma)$ plotted in double logarithmic scale in Fig. 6b has been fitted by the theoretical scaling law $\Lambda = K \cdot Ma^{-1.57}$, with a fitting parameter K that takes the values $K=(2.0\pm0.2)\times10^5$, $(4.4\pm0.4)\times10^5$ and $(8.9\pm0.8)\times10^5$ for

θ=9%, 19% and 36%, respectively. The theoretical scaling law seems to correctly fit the experimental data. The pre-factor K at $Ma^{-11/7}$ in Eq. (12) is expected to increase with increasing θ values since the maximal agglomerate thickness D_{max} increases with θ, while the agglomeration timescale τ_a is considered to globally decrease with θ according to our experiments on agglomeration kinetics in quiescent suspensions. Thus, the model seems to predict an increasing dependence of the capture efficiency on the surface coverage in qualitative agreement with experiments. Again, quantitative predictions of Λ as function of θ are hardly possible because of large imprecision in evaluation of D_{max} and indefiniteness of the numerical pre-factors omitted in the considered scaling law [Eq. (12)].

From the practical point of view, we learn that the capture efficiency of IONP and the retention capacity of the magnetic microfluidic separator (characterized by the maximum deposit area) are considerably enhanced (from zero at θ=0 up to $s_{max}\approx$8 at θ=36%) by adsorption of MB molecules, as long as this adsorption promotes the primary and secondary agglomeration.

CONCLUSIONS

The series of the two papers (Parts I and II) is devoted to elucidation of the effect of molecular adsorption on the surface of magnetic (maghemite) IONP on the enhancement of their field-induced (secondary) agglomeration and magnetic separation due to screening of the repulsive interactions between nanoparticles that involves their primary agglomeration in the absence of magnetic fields. Figure 7 depicts a schematic representation of the considered scenario of enhancement of magnetic separation by molecular adsorption.

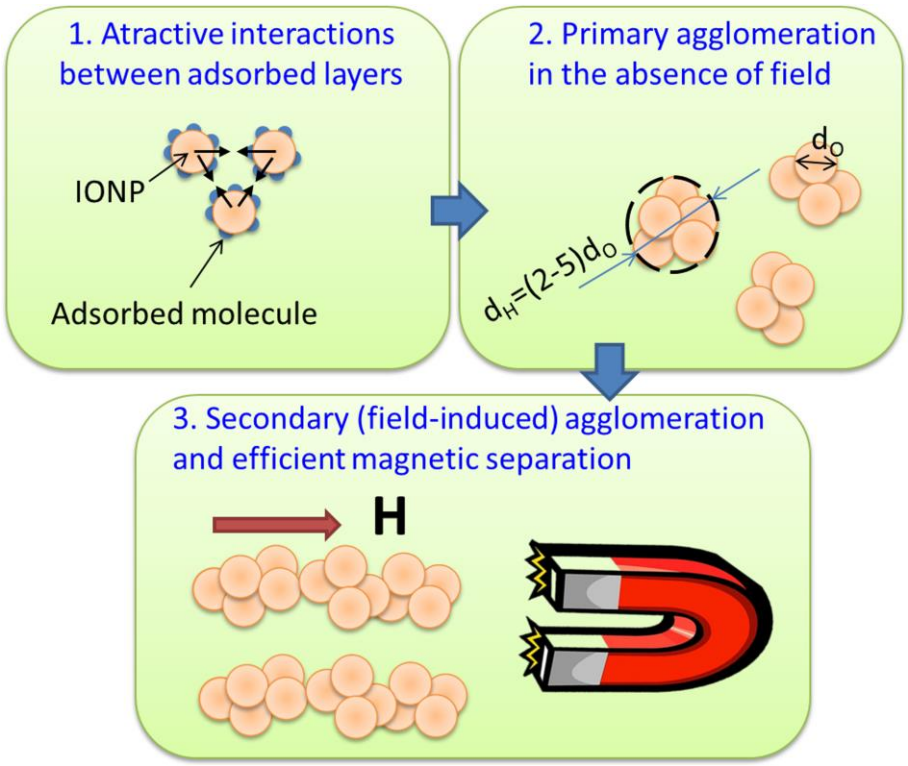

Fig. 7. Schematic representation of the mechanism of magnetic separation enhancement by molecular adsorption

The mechanisms of adsorption-induced primary agglomeration are considered in the companion paper[21] (Part I) on a particular example of methylene blue (MB) cationic dye adsorbed on citrate-

coated IONP surface. Based on this experimental system, the present paper (Part II) considers the complex phenomenon of adsorption-enhanced magnetic separation from the general perspective, i.e. without regard to particular physicochemical mechanisms by which the primary agglomeration is induced as the molecules are progressively adsorbed onto IONP surface. The results of the present study can be summarized as follows:

(1) The phase diagram of the field-induced phase separation (secondary agglomeration) seems to be solely governed by the magnetic field parameter $\alpha \sim \mu_0 H^2 \langle d_H \rangle^3 / (k_B T)$, which elucidates the decreasing trend of the agglomeration threshold with progressive molecular adsorption through the increase of the magnetic energy of the primary agglomerates (varying as the cube of their hydrodynamic size $<d_H>$) with increasing θ.

(2) The final size of the field-induced secondary agglomerates seems to be totally governed by the suspension initial supersaturation Δ_0, progressively increasing with the surface coverage θ and leading to larger agglomerates for higher θ values. The effect of the surface coverage θ on the timescale τ_a of the secondary agglomeration is less evident, since it decreases with Δ_0 ($\tau_a \propto \Delta_0^{-1}$, leading to accelerated kinetics with growing θ) and decreases with the effective diffusivity of primary agglomerates ($\tau_a \propto D_{eff}^{-1}$, leading to slowing down of agglomeration with θ). The first mechanism seems to dominate.

(3) The magnetic separation of MB/IONP mixtures in a microfluidic channel equipped with a magnetizable micropillar is strongly enhanced by the field-induced agglomeration occurring when the suspension travels through a long connecting tubing towards the micropillar, while the secondary (field-induced) agglomeration, in turn, is strongly amplified by the primary agglomeration due to molecular adsorption onto the IONP surface. The magnetic separation enhancement is revealed through a substantial increase of the size of the IONP deposits around the micropillar and the increase of the flux of the captured nanoparticles (characterized by the capture efficiency Λ) with increasing surface coverage θ. A semi-empirical model predicts that the capture efficiency is governed by the Mason number *Ma* and, to a lesser extent, by the magnetic field parameter α ($\Lambda \propto \alpha^{-4/7} Ma^{-11/7}$). Furthermore, Λ decreases with the agglomeration timescale ($\Lambda \propto \tau_a^{-4/7}$) and increases with the thickness of the secondary agglomerates ($\Lambda \propto D_{\max}^{2}$) leading to a substantial increase with the surface coverage θ, in agreement with experimental results.

In a real application, one could use compact serpentine microfluidic channels instead of long connecting tubing in order to induce the secondary agglomeration of the primary agglomerates before they arrive to the micropillar.

These conclusions allow us to establish the cause-and-effect relation between the θ parameter and the efficiency of field-induced agglomeration or magnetic separation, which can be schematized as follows:

$$\theta \nearrow \longrightarrow \langle d_H \rangle \nearrow \longrightarrow \alpha \nearrow \longrightarrow \Delta_0 \nearrow \longrightarrow \begin{pmatrix} L_{max}, D_{max} \nearrow \\ \tau_a \searrow \end{pmatrix} \longrightarrow \Lambda \nearrow$$

with $\nearrow$ and $\searrow$ symbols on the right of each physical quantity standing for an increase or a decrease of the given quantity.

These behaviors are expected to apply to other "magnetic adsorbent/ molecular adsorbate" pairs, as long as the primary agglomerate size $<d_H>$ is known as function of the surface coverage θ,

no matter the reason for primary agglomeration, provided that: (a) colloidal attractive interactions are of a shorter range than the magnetic ones, and (b) the timescales of the field-induced processes are much shorter than those of the primary agglomeration. For instance, similar effects have recently been observed for adsorption of curcumin molecules to β-cyclodextrin coated IONP when the adsorption was governed by hydrophobic host-guest interactions and induced a strong primary and secondary (field-induced) agglomeration of IONP, as will be reported in a forthcoming paper.

From the general perspective, the present paper is believed to contribute to the understanding of magnetic nanoparticle separation under magnetophoresis – the phenomenon used in different biomedical and engineering applications (see review by Leong at al.[29] and the references therein). Furthermore, some similarity can be found between magnetophoresis of agglomerated nanoparticles reported in the present paper and electrophoresis of agglomerated colloids in electrokinetic soil remediation[48,49]. Finally, adsorption-induced agglomeration and magnetic field-induced agglomeration of IONP (described in Parts I and II) are phenomena belonging to a vast family of stimuli-responsive self-assembly of nanoparticles.[50,51]

ASSOCIATED CONTENT

Supporting Information. Physicochemical characterization of the ferrofluid samples; Sketch of the microfluidic channel; Full panel of the snapshots showing field-induced (secondary) IONP agglomeration and magnetic separation on a magnetized micropillar; Size distribution histograms of the secondary agglomerates; Time dependencies of the size of the nanoparticle deposits around the micropillar.

ACKNOWLEDGEMENTS

PK, CL, CH and GG acknowledge the French 'Agence Nationale de la Recherche', Project Future Investments UCA JEDI, No. ANR-15-IDEX-01 (projects MANTRA, ImmunoMag and MagFilter) and the private company Axlepios Biomedical for financial support, JQC acknowledges the financial support of UCA JEDI and Axlepios Biomedical through the PhD fellowship; BLCF acknowledges Erasmus Mundus through its mobility fellowship.

REFERENCES

1. Douziech-Eyrolles, L.; Marchais, H.; Herve, K.; Munnier, E.; Souce, M.; Linassier, C.; Dubois, P.; Chourpa, I. Nanovectors for anticancer agents based on superparamagnetic iron oxide nanoparticles. *Int. J. Nanomed*. **2007**, *2*, 541–550.
2. Liu, T. Y.; Hu, S. H.; Liu, K. H.; Shaiu, R. S.; Liu, D. M.; Chen, S. Y. Instantaneous drug delivery of magnetic/thermally sensitive nanospheres by a high-frequency magnetic field. *Langmuir* **2008**, *24*, 13306-13311.
3. Cao, Z.; Yue, X.; Li, X.; Dai, Z. Stabilized magnetic cerasomes for drug delivery. *Langmuir* **2013**, 29, 14976-14983.
4. Hergt, R.; Dutz, S.; Müller, R.; Zeisberger, M. Magnetic particle hyperthermia: nanoparticle magnetism and materials development for cancer therapy. *J. Phys.: Condens. Matter* **2006**, *18*, S2919-S2934.
5. Béalle, G.; Di Corato, R.; Kolosnjaj-Tabi, J.; Dupuis, V.; Clément, O.; Gazeau, F.; Wilhelm, C.; Ménager, C. Ultra magnetic liposomes for MR imaging, targeting, and hyperthermia. *Langmuir* **2012**, *28*, 11834-11842.
6. Rümenapp, C.; Gleich, B.; Haase, A. Magnetic nanoparticles in magnetic resonance imaging and diagnostics. *Pharmaceutical Research* **2012**, *29*, 1165-1179.
7. Scherer, F.; Anton, M.; Schillinger, U.; Henke, J.; Bergemann, C.; Krüger, A.; Gänsbacher, B.; Plank, C. Magnetofection: enhancing and targeting gene delivery by magnetic force in vitro and in vivo. *Gene therapy* **2002**, *9*, 102-109.

8. Arsianti, M.; Lim, M.; Marquis, C. P.; Amal, R. Assembly of polyethylenimine-based magnetic iron oxide vectors: insights into gene delivery. *Langmuir* **2010**, *26*, 7314-7326.
9. Yavuz, C. T.; Prakash, A.; Mayo, J. T.; Colvin, V. L. Magnetic separations: from steel plants to biotechnology. *Chem. Eng. Sci*. **2009**, *64*, 2510-2521.
10. Ambashta, R. D.; Sillanpää, M. Water purification using magnetic assistance: a review. *J. Hazard. Mater*. **2010**, *180*, 38-49.
11. Mudassir, M. A.; Hussain, S. Z.; Jilani, A.; Zhang, H.; Ansari, T. M.; Hussain, I. Magnetic hierarchically macroporous emulsion-templated poly (acrylic acid)–iron oxide nanocomposite beads for water remediation. *Langmuir* **2019**, *35*, 8996-9003.
12. Guibert, C.; Dupuis, V.; Peyre, V.; Fresnais, J. Hyperthermia of magnetic nanoparticles: experimental study of the role of aggregation. *J. Phys. Chem. C* **2015**, 119, 28148-28154.
13. Etheridge, M. L.; Hurley, K. R.; Zhang, J.; Jeon, S.; Ring, H. L.; Hogan, C.; Haynes, Ch. L.; Garwood, M.; Bischof, J. C. Accounting for biological aggregation in heating and imaging of magnetic nanoparticles. *Technology* **2014**, *2*, 214-228.
14. Eberbeck, D.; Kettering, M.; Bergemann, C.; Zirpel, P.; Hilger, I.; Trahms, L. Quantification of the aggregation of magnetic nanoparticles with different polymeric coatings in cell culture medium. *J. Phys. D: Appl. Phys.* **2010**, *43*, 405002.
15. Cabrera, D.; Camarero, J.; Ortega, D.; Teran, F. J. Influence of the aggregation, concentration, and viscosity on the nanomagnetism of iron oxide nanoparticle colloids for magnetic hyperthermia. *J Nanopart. Res*. **2015**, *17*, 121.
16. Pilati, V.; Gomide, G.; Gomes, R. C.; Goya, G. F.; Depeyrot, J. Colloidal Stability and Concentration Effects on Nanoparticle Heat Delivery for Magnetic Fluid Hyperthermia. *Langmuir* **2021**, *37*, 1129-1140.
17. Costo, R.; Bello, V.; Robic, C.; Port, M.; Marco, J. F.; Puerto Morales, M.; Veintemillas-Verdaguer, S. Ultrasmall iron oxide nanoparticles for biomedical applications: improving the colloidal and magnetic properties. *Langmuir* **2012**, *28*, 178-185.
18. Liu, S.; Han, Y.; Qiao, R.; Zeng, J.; Jia, Q.; Wang, Y.; Gao, M. Investigations on the interactions between plasma proteins and magnetic iron oxide nanoparticles with different surface modifications. *J. Phys. Chem. C* **2010**, *114*, 21270-21276.
19. Lartigue, L.; Wilhelm, C.; Servais, J.; Factor, C.; Dencausse, A.; Bacri, J. C.; Luciani, N.; Gazeau, F. Nanomagnetic sensing of blood plasma protein interactions with iron oxide nanoparticles: impact on macrophage uptake. *ACS Nano* **2012**, *6*, 2665-2678.
20. Jedlovszky-Hajdú, A.; Bombelli, F. B.; Monopoli, M. P.; Tombacz, E.; Dawson, K. A. Surface coatings shape the protein corona of SPIONs with relevance to their application in vivo. *Langmuir* **2012**, *28*, 14983-14991.
21. Talbot D.; Queiros Campos, J.; Checa-Fernandez, B.L.; Marins, J.A.; Lomenech, C.; Hurel, Ch.; Godeau, G.; Raboisson-Michel, M.; Verger-Dubois, G.; Obeid, L.; Kuzhir, P.; Bee, A. Adsorption of organic dyes on magnetic iron oxide nanoparticles. Part I: Mechanisms and adsorption-induced nanoparticle agglomeration. *ACS Omega* **2021**, *6*, 19086-19098.
22. Evans, D. F.; Wennerstrom, H. *The Colloidal Domain - where physics, chemistry, biology, and technology meet*, 2nd ed.; Wiley-VCH: USA, 1999.
23. Swan, J. W.; Vasquez, P. A.; Whitson, P. A.; Fincke, E. M.; Wakata, K.; Magnus, S. H.; De Winne, F.; Barratt, M.R.; Agui, J.H; Green, R.D.; Hall, N.R.; Bohman, D.Y.; Bunnell, C.T.; Gast, A.P.; Furst E.M. Multi-scale kinetics of a field-directed colloidal phase transition. *Proc. Nat. Acad. Sci*. **2012**, *109*, 16023-16028.
24. Socoliuc, V.; Vékás, L.; Turcu, R. Magnetically induced phase condensation in an aqueous dispersion of magnetic nanogels. *Soft Matter* **2013**, *9*, 3098-3105.
25. Ezzaier, H.; Alves Marins, J.; Razvin, I.; Abbas, M.; Ben Haj Amara, A.; Zubarev, A.; Kuzhir, P. Two-stage kinetics of field-induced aggregation of medium-sized magnetic nanoparticles. *J. Chem. Phys*. **2017**, *146*, 114902.
26. Mohapatra, D. K; Philip, J. Effect of surface charge screening on critical magnetic fields during field induced structural transitions in magnetic fluids. *J. Appl. Phys*. **2019**, *125*, 244301.
27. Kim, H.; Sau, M.; Furst, E. M. An expanded state diagram for the directed self-assembly of colloidal suspensions in toggled fields. *Langmuir* **2020**, *36*, 9926–9934.
28. Kuzhir, P.; Magnet, C.; Ezzaier, H.; Zubarev, A.; Bossis, G. Magnetic filtration of phase separating ferrofluids: From basic concepts to microfluidic device. *J. Magn. Magn. Mater*. **2017**, *431*, 84-90.
29. Leong, S. S.; Ahmad, Z.; Low, S. C.; Camacho, J.; Faraudo, J.; Lim, J. Unified View of Magnetic Nanoparticle Separation under Magnetophoresis. *Langmuir* **2020**, *36*, 8033-8055

30. Szekeres, M.; Tóth, I. Y.; Illés, E.; Hajdú, A.; Zupkó, I.; Farkas, K.; Oszlánczi G.; Tiszlavicz, L.; Tombácz, E. Chemical and colloidal stability of carboxylated core-shell magnetite nanoparticles designed for biomedical applications. *Int. J Molecular Sci*. **2013**, *14*, 14550-14574.
31. Ezzaier, H.; Marins, J. A.; Claudet, C.; Hemery, G.; Sandre, O.; Kuzhir, P. Kinetics of aggregation and magnetic separation of multicore iron oxide nanoparticles: effect of the grafted layer thickness. *Nanomaterials* **2018**, 8, 623.
32. Massart R. Preparation of aqueous magnetic liquids in alkaline and acidic media. *IEEE Trans. Magn*. **1981**, *17*, 1247–1248.
33. Buyevich, Y. A.; Ivanov, A. O. Equilibrium properties of ferrocolloids. *Physica A* **1992**, *190*, 276-294.
34. Hynninen, A. P.; Dijkstra, M. Phase diagram of dipolar hard and soft spheres: Manipulation of colloidal crystal structures by an external field. *Phys. Rev. Lett*. **2005**, *94*, 138303.
35. Sherman, Z. M.; Rosenthal, H.; Swan, J. W. Phase separation kinetics of dynamically self-assembling nanoparticles with toggled interactions. *Langmuir* **2018**, *34*, 1029-1041.
36. Rosensweig, R. E. *Ferrohydrodynamics;* Cambridge University Press, Cambridge: UK, 1985.
37. Magnet, C.; Kuzhir, P.; Bossis, G.; Meunier, A.; Nave, S.; Zubarev, A.; Lomenech, C.; Bashtovoi, V. Behavior of nanoparticle clouds around a magnetized microsphere under magnetic and flow fields. *Phys. Rev. E* **2014**, *89*, 032310.
38. Szalai, I.; Nagy, S.; Dietrich, S. Linear and nonlinear magnetic properties of ferrofluids. *Phys. Rev. E* **2015**, *92*, 042314.
39. Kuzhir, P.; Raboisson-Michel, M.; Queiros Campos, J.; Verger-Dubois, G.; Zubarev, A. Yu. Unified mathematical model of the kinetics of nanoparticle phase condensation in magnetic fields. *Math. Meth. Appl. Sci*. **2020**, 1-13; DOI: 10.1002/mma.6739.
40. Laskar, J. M.; Philip, J.; Raj, B. Experimental investigation of magnetic-field induced aggregation kinetics in nonaqueous ferrofluids. *Phys. Rev. E* **2010**, *82*, 021402.
41. Vinod, S.; Philip, J. Experimental evidence for the significant role of initial cluster size and liquid confinement on thermo-physical properties of magnetic nanofluids under applied magnetic field. *J. Mol. Liq*. **2018**, *257*, 1–11.
42. Ivanov, A. O.; Novak, E. V. Phase separation of ferrocolloids: The role of van der Waals interaction. *Colloid J.* **2007**, *69*, 302-311.
43. Ezzaier, H.; Marins, J. A.; Schaub, S.; Amara, B. H.; Kuzhir, P. Capture of magnetic nanoparticles on ordered magnetizable arrays: A parametric study. *J. Magn. Magn. Mater*. **2018**, *459*, 350-355.
44. van de Ven, T. G. M. *Colloidal Hydrodynamics,* Academic Press; London: UK, 1989.
45. Zubarev, A. Y.; Ivanov, A. O. Kinetics of a magnetic fluid phase separation induced by an external magnetic field. *Phys. Rev. E* **1997**, *55*, 7192-7202.
46. Raboisson-Michel, M.; Queiros Campos, J.; Schaub, S.; Zubarev, A.; Verger-Dubois, G.; Kuzhir, P. Kinetics of field-induced phase separation of a magnetic colloid under rotating magnetic fields. *J. Chem. Phys*. **2020**, *153*, 154902.
47. Orlandi, G.; Kuzhir, P.; Izmaylov, Y.; Marins, J. A.; Ezzaier, H.; Robert, L.; Doutre F.; Noblin X.; Lomenech, C.; Bossis G.; Meunier A.; Sandoz, G.; Zubarev, A. Microfluidic separation of magnetic nanoparticles on an ordered array of magnetized micropillars. *Phys. Rev. E* **2016**, *93*, 062604.
48. Virkutyte, J.; Sillanpää, M.; Latostenmaa, P. Electrokinetic soil remediation—critical overview. *Sci. Total Environ*. **2002**, *289*, 97-121.
49. Cheng, F.; Guo, S.; Li, G.; Wang, S.; Li, F.; Wu, B. The loss of mobile ions and the aggregation of soil colloid: Results of the electrokinetic effect and the cause of process termination. *Electrochim. Acta* **2017**, *258*, 1016-1024.
50. Grzelczak, M.; Liz-Marzán, L. M.; Klajn, R. Stimuli-responsive self-assembly of nanoparticles. *Chem. Soc. Rev*. **2019**, *48*, 1342-1361.
51. Hwang, E. Y.; Lee, J. S.; Lim, D. W. Oppositely Charged, Stimuli-Responsive Anisotropic Nanoparticles for Colloidal Self-Assembly. *Langmuir* **2019**, *35*, 4589-4602.

Table of Contents graphic